Hydroclimatic extremes contribute to asymmetric trends in ecosystem productivity loss

Jun Li, Emanuele Bevacqua, Zhaoli Wang, Stephen Sitch, Vivek Arora, Almut Arneth, Atul K Jain, Daniel Goll, Hanqin Tian, Jakob Zscheischler

communications earth & environment

ARTICLE

https://doi.org/10.1038/s43247-023-00869-4 OPEN

Hydroclimatic extremes contribute to asymmetric trends in ecosystem productivity loss

Jun Li[1,2], Emanuele Bevacqua[1], Zhaoli Wang[2], Stephen Sitch[3], Vivek Arora[4], Almut Arneth[5], Atul K. Jain[6], Daniel Goll[7], Hanqin Tian[8] & Jakob Zscheischler[1✉]

Gross primary production is the basis of global carbon uptake. Gross primary production losses are often related to hydroclimatic extremes such as droughts and heatwaves, but the trend of such losses driven by hydroclimatic extremes remains unclear. Using observationally-constrained and process-based model data from 1982-2016, we show that drought-heat events, drought-cold events, droughts and heatwaves are the dominant drivers of gross primary production loss. Losses associated with these drivers increase in northern midlatitude ecosystem but decrease in pantropical ecosystems, thereby contributing to around 70% of the variability in total gross primary production losses. These asymmetric trends are caused by an increase in the magnitude of gross primary production losses in northern midlatitudes and by a decrease in the frequency of gross primary production loss events in pantropical ecosystems. Our results suggest that the pantropics may have become less vulnerable to hydroclimatic variability over recent decades whereas gross primary production losses and hydroclimatic extremes in northern midlatitudes have become more closely entangled.

[1] Department of Computational Hydrosystems, Helmholtz Centre for Environmental Research–UFZ, Leipzig, Germany. [2] School of Civil Engineering and Transportation, State Key Laboratory of Subtropical Building Science, South China University of Technology, Guangzhou, China. [3] Department of Geography, College of Life and Environmental Sciences, University of Exeter, Exeter, UK. [4] Canadian Centre for Climate Modelling and Analysis, Environment and Climate Change Canada, Victoria, BC, Canada. [5] Institut für Meteorologie und Klimaforschung (IMK), Karlsruher Institut für Technologie (KIT), Karlsruhe, Germany. [6] Department of Atmospheric Sciences, University of Illinois, Urbana, IL, USA. [7] Université Paris Saclay, CEA-CNRS-UVSQ, LSCE/IPSL, Gif sur Yvette, France. [8] Department of Earth and Environmental Sciences, Schiller Institute for Integrated Science and Society, Boston College, Chestnut Hill, MA, USA. ✉email: jakob.zscheischler@ufz.de

The terrestrial ecosystem is an essential component of the current global carbon sink[1], sequestering around one-third of the annual anthropogenic carbon emissions and therefore mitigates the increase in atmospheric CO_2 concentration and the associated global warming[2]. Terrestrial gross primary production (GPP), the total amount of CO_2 fixed by plants via photosynthesis, is the largest global carbon flux driving the net carbon balance of the terrestrial ecosystem[3, 4]. However, terrestrial ecosystems are adapted to a limited range of hydroclimatic conditions and GPP is highly sensitive to hydroclimatic extremes, which can cause persistent GPP reductions[5, 6].

Droughts, extremely wet conditions, heatwaves and cold spells, as well as the corresponding compound hydroclimatic events (e.g., compound drought-heat events) are commonly studied climate extremes[7]. These hydroclimatic extremes are one of the major contributors to GPP variability, via water scarcity, soil waterlogging, thermal stress, hypoxic conditions, and frost damage[8]. Changes in frequency and intensity of hydroclimatic extremes are one consequence of global climate change[9–11]. For instance, the water vapor content of the atmosphere has increased over the past few decades due to global warming, affecting the global hydrological cycle[12]. Consequently, changes in hydroclimatic extremes can impact GPP and hence the terrestrial carbon sink[13, 14]. Most studies have concluded that the occurrence of severe droughts or heatwaves generally decreased GPP on a regional or global scale[15–18]. In addition, GPP losses arising from compound drought-heat events usually outpace those of individual droughts or heatwaves[19–21]. Recently, the risk and cumulative effects of drought on global GPP have been investigated[22, 23]. Overall, these research results confirm the close relationship between GPP losses and hydroclimatic extremes. Cold spells and extreme wetness are another type of climate extreme that can affect vegetation growth and photosynthesis. The GPP responses to cold spells and extreme wetness has attracted some attention, given that such events still occur frequently, despite ongoing global warming[24, 25]. The ample evidence of systematic impacts from hydroclimatic extremes raises concerns about whether hydroclimatic extremes have contributed to a shift in GPP losses across regional and global scales. However, the conclusions regarding the trend in GPP response to hydroclimatic extremes are uncertain due to the varying sensitivities of terrestrial ecosystems to hydroclimatic extremes[26–29]. For instance, some studies have shown an increase in drought-induced GPP losses and drought-sensitive areas in the vast northern regions[4, 30], while others have suggested a weakened drought impacts in some wet regions[31, 32]. Furthermore, which extreme events are significantly associated with GPP losses remain unclear. Therefore, it is relevant to thoroughly study the effects of hydroclimatic extremes on changes in GPP losses during last three decades, which is critical for deepening our understanding of the terrestrial carbon cycle and its future evolution.

Here, we investigated the role of hydroclimatic extremes on global GPP losses over the last three and a half decades. We attributed the GPP losses to drought, wet extremes, heat, cold extremes, and corresponding compound hydroclimatic events based on the coincidence of significant climate anomalies (Methods). We employed long-term (1982–2016) observationally-constrained and state-of-the-art modeled GPP products produced with different approaches, including light use efficiency (LUE)[33], near-infrared reflectance (NIRv)[34], upscaled eddy covariance flux tower measurements (FLUXCOM)[35], and an ensemble of 12 dynamic global vegetation models (DGVMs)[36]. We used two compound event indices to characterize compound hydroclimatic conditions (i.e., drought-heat extreme, drought-cold extreme, wet-cold extreme, and wet-heat extreme). In general, drought and wet extremes were identified via soil moisture from the Global Land Evaporation Amsterdam Model, the Global Land Data Assimilation System (GLDAS), and ECMWF Reanalysis v5, while heat and cold extremes were identified by temperature (Methods).

Result

GPP losses associated with hydroclimatic extremes. We quantified the GPP losses attributed to hydroclimatic extremes across the globe during 1982–2016. Globally, GPP losses show a strong association with a variety of hydroclimatic extremes. Drought-heat extremes explain the largest contribution to global GPP losses (30.9 ± 5.1%), followed by droughts (29.9 ± 5.2%), drought-cold extremes (27.9 ± 3.4%), heat extremes (24.2 ± 2.8%), and cold extremes (16.8 ± 2.1%) (Fig. 1a). In contrast, wet-heat extremes, wet-cold extremes, and wet extremes are not significantly related to GPP losses at the global scale, explaining 13.7 ± 2.0%, 13.1 ± 2.6%, and 11.1 ± 2.6% of the global GPP losses, respectively (Fig. 1a). The GPP losses associated with hydroclimatic extremes show clear spatial patterns. Drought-heat, drought, and heat extremes cause widespread negative effects, and the corresponding hotspots of their impacts are predominantly situated in mid-to-low latitudes (Fig. 1b, c, e). The effects of wet-cold and wet extremes are mostly localized in boreal northern high latitudes (Fig. 1h, i). Areas associated with cold extremes mainly occur in northern high latitudes and eastern Asia (Fig. 1f). Notably, drought-cold impacts are widely distributed in much of the global land (Fig. 1d), while wet-heat impacts are scattered in southern America and central Africa (Fig. 1g).

All the above results based on GPP and extreme indices with linear trends removed are similar when employing GPP and indices with non-linear trends removed and utilizing different soil moisture products (Supplementary Figs. S1–3). Taken together, drought-heat, drought, drought-cold, and heat extremes are identified as the dominant hydroclimatic extremes causing GPP losses over large areas of the global land, indicating the dominant adverse impact of these hydroclimatic extremes on global terrestrial carbon uptake.

Given the strong seasonality and regionality of the response of GPP to hydroclimatic variations[24], we investigated the latitudinal and monthly patterns of GPP losses associated with hydroclimatic extremes (Supplementary Fig. S4). The highest GPP losses related to each extreme is mainly concentrated at mid-to-low latitudes. Furthermore, the effect of hydroclimatic extremes on GPP shows a clear temporal pattern. In the northern mid-to-low latitudes, GPP losses associated with hydroclimatic extremes predominantly occur during the growing season (i.e., May to September), while in the pantropics, hydroclimatic extremes cause higher GPP losses during wet season months (i.e., January–April and October–December).

Trends in GPP loss associated with hydroclimatic extremes. Next, we assessed trends in the magnitude of GPP losses associated with hydroclimatic extremes over recent decades. Since high GPP losses mostly occur in the global mid-to-low latitudes, where drought-heat, drought-cold, drought, and heat extremes are the dominant drivers (Fig. 1 and Supplementary Fig. S4), we investigated GPP loss trends associated with these hydroclimatic extremes. Globally, GPP losses associated with drought-cold extremes present an intensification, while GPP losses related to drought and heat show little changes (Supplementary Fig. S5). In general, the spatial pattern of the losses shows both increasing and decreasing trends. Areas of increasing trends of GPP losses are broadly situated in northern midlatitudes, whereas areas with decreasing trends are more localized in the pantropics (Supplementary Fig. S5).

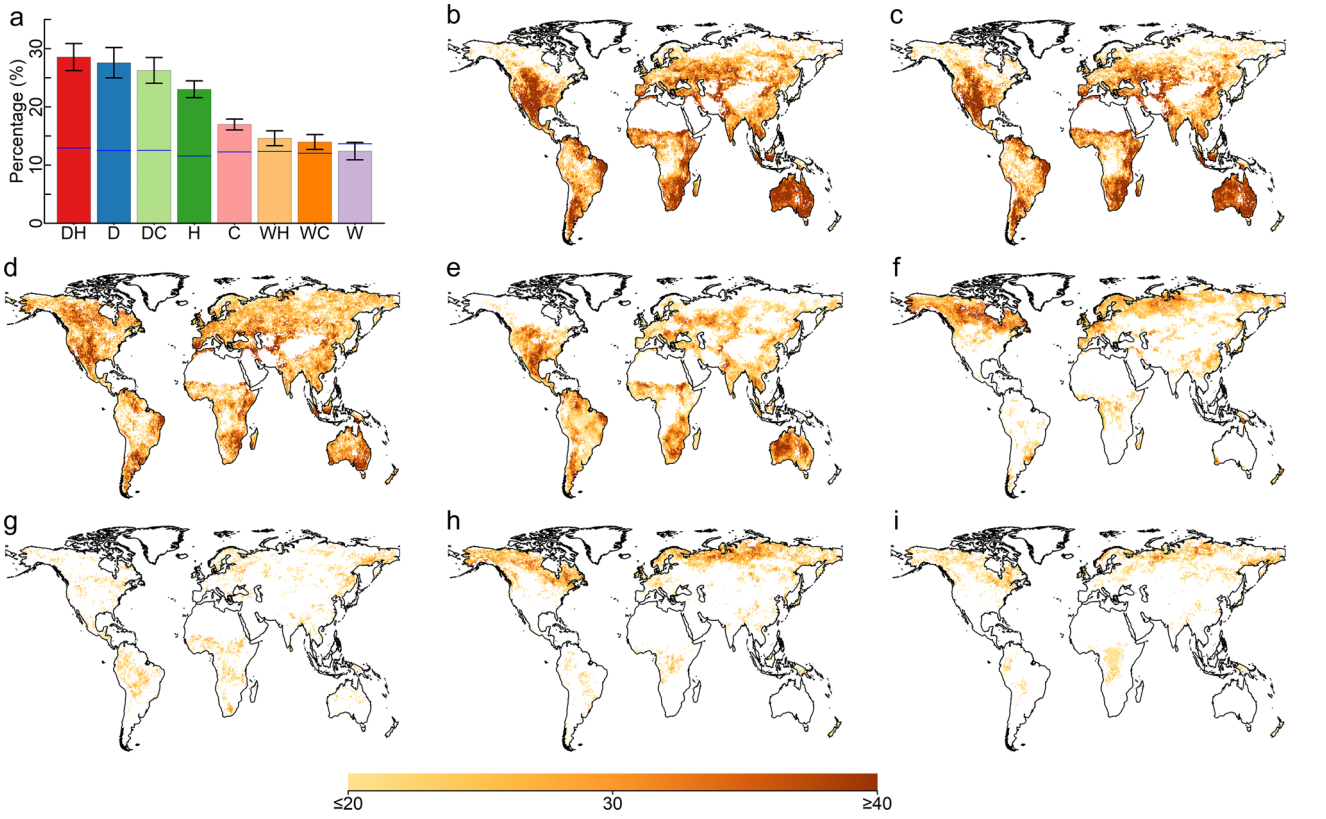

Fig. 1 GPP losses attributed to hydroclimatic extremes during 1982-2016. a Fraction (%) of global GPP losses associated with drought-heat extremes (DH), drought (D), drought-cold extremes (DC), heat extremes (H), cold extremes (C), wet-heat extremes (WH), wet-cold extremes (WC), and wet extremes (W). The spatial pattern of GPP losses associated with drought-heat extremes (**b**), drought (**c**), drought-cold extremes (**d**), heat extremes (**e**), cold extremes (**f**), wet-heat extremes (**g**), wet-cold extremes (**h**), and wet extremes (**i**). In (**a**), the bar show values averaged over all GPP datasets, and the error bars indicate one standard deviation between GPP products; blue lines within the bar indicate the 0.05 significant level. In (**b**–**i**), values for which less than half of the products are significant at the 0.1 level are masked in white. The results are based on GPP products and extreme indices with the removed linear trends as well as GLEAM soil moisture.

We then performed a regional analysis, focusing on the northern midlatitudes (23.5-65°N) and pantropics (23.5°S-23.5°N), which play important roles in regulating the global carbon cycle and atmospheric CO_2 concentration[13, 37]. In both regions, drought-heat, drought-cold, drought, and heat extremes are the dominant drivers of GPP losses (Fig. 2a, b). Specifically, 52.1 ± 4.1% and 55.2 ± 6.6% of GPP losses are associated with these extremes in the northern midlatitudes and pantropics, respectively, implying strong impacts of these hydroclimatic extremes on GPP losses[20, 38]. The GPP losses associated with the identified dominant drivers have asymmetrical trends in the two regions, with losses increasing in northern midlatitudes (Fig. 2c) but decreasing across the pantropics (Fig. 2d). We further investigate how well the trends from dominant drivers determine regional GPP losses. For the two focus-regions, the trends of regional total GPP losses are strongly correlated with the trends of GPP losses attributed to these extreme drivers across GPP datasets ($P < 0.01$), explaining about 66% and 82% of the variance in total trends in the northern midlatitudes and pantropics, respectively (Fig. 2e, f). These results suggest that these hydroclimatic extremes contribute primarily to the rising adverse impacts on plant productivity in the northern midlatitudes and the weakening impacts across the pantropics.

Results are similar when using GPP products and indices with removed non-linear trends, different moving windows, and different soil moisture products (Supplementary Figs. S6–10). Taken together, drought-heat, drought-cold, drought, and heat extremes play a dominant role in increasing and decreasing GPP losses across the northern midlatitudes and pantropics over the last three decades, respectively.

The identified asymmetry may be related to changes in the frequency of GPP loss associated with the dominant drivers or changes in the magnitude of GPP loss per event associated with the dominant drivers. We disentangled these effects (Methods) and find that in the northern midlatitudes, datasets that exhibit strongly enhanced GPP losses associated with dominant drivers show a strong strengthening of event-based GPP loss related to the dominant drivers ($r^2 = 0.71$; $P < 0.01$, Fig. 3a). Changes in the frequency of GPP loss associated with dominant drivers only contribute weakly ($r^2 = 0.22$) (Fig. 3b). In contrast, the weakening GPP losses in pantropics are strongly associated with the decrease in the frequency of event-based GPP loss ($r^2 = 0.65$; $P < 0.01$, Fig. 3c). Here, the magnitude of each GPP loss event related to dominant drivers does not explain any variation across datasets ($r^2 = 0.00$) (Fig. 3d). We again used GPP products and indices with removed non-linear trends, different moving windows, and different soil moisture products (Supplementary Figs. S11–15), and found similar results. These analyses suggests that an intensification of GPP losses in northern midlatitudes is induced by an increase in the magnitude of each event-based GPP loss, while a decrease in GPP losses in the pantropics is caused by the reduction in frequency of event-based GPP loss.

We also analyzed seasonal trends of GPP losses associated with hydroclimatic extremes in the two regions. A consistent large increase in GPP losses associated with drought-heat, drought, and heat extremes is found from June to August in northern

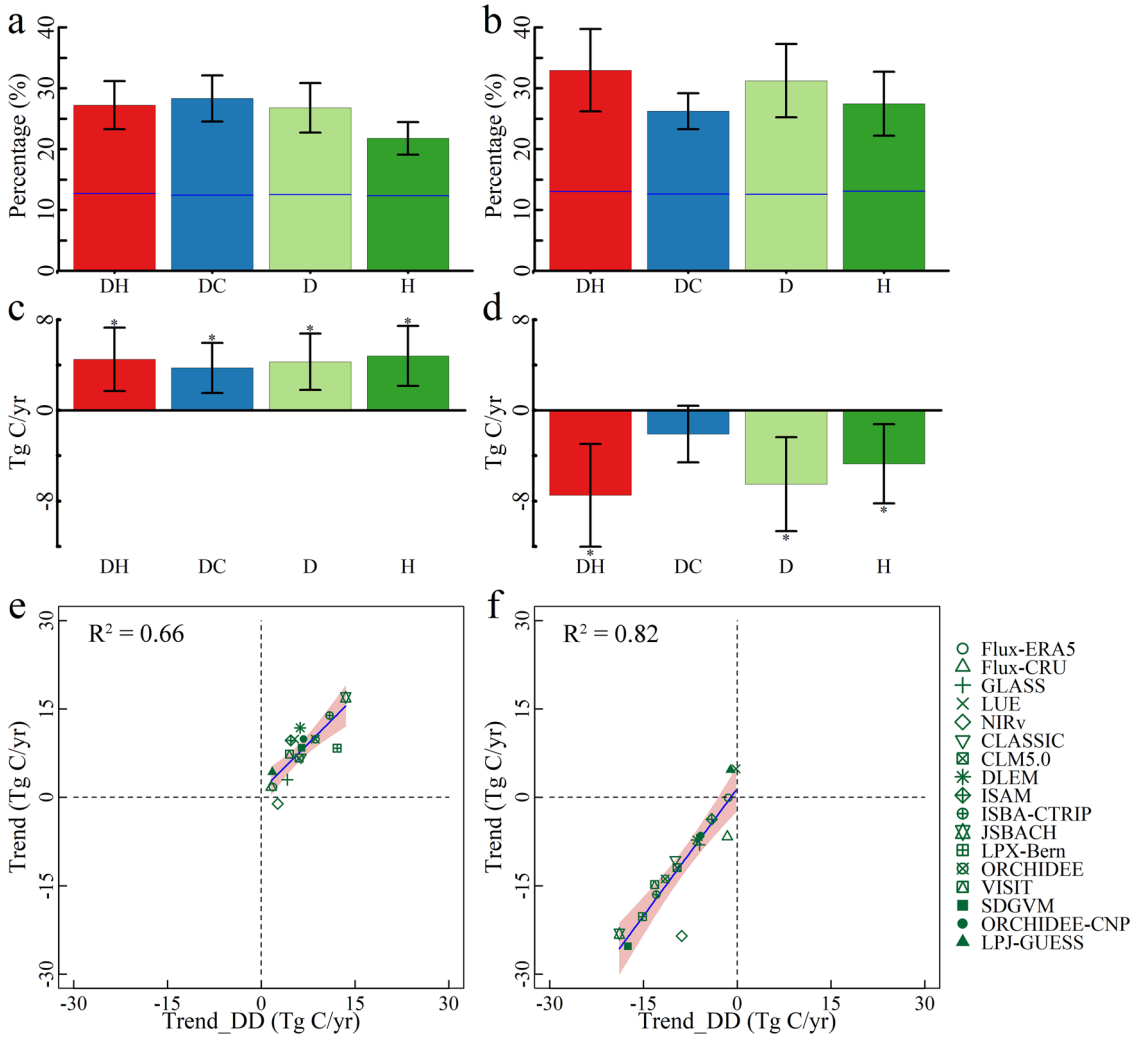

Fig. 2 Asymmetric changes in GPP losses attributed to hydroclimatic extremes between northern midlatitude and pantropical ecosystems. **a** Percentage of GPP losses attributed to each dominant extreme hydroclimatic driver relative to total GPP losses in northern midlatitudes (23.5-65°N). Dominant extreme hydroclimatic drivers are drought-heat extremes (DH), drought-cold extremes (DC), drought (D), and heat extremes (H). **c** Trends of GPP losses associated with dominant drivers in northern midlatitudes. **e** Trends of GPP losses associated with dominant drivers (*x*-axis) against that of total GPP losses (*y*-axis) for each dataset. **b, d, f** The same as (**a, c, d**) but for pantropics (23.5°S-23.5°N). In (**a**, **b**), blue lines within the bar indicate the 0.05 significant level. In (**c**, **d**), positive trends indicate an increase in GPP loss, and vice versa for negative trends; the * indicates that the ensemble Z-values of Mann-Kendall are at the 0.05 significant level. In (**e**) and (**f**), the shaded areas indicate one standard deviation and the blue lines are the fitting curves according to the trends of GPP losses associated with dominant drivers (Trend_DD) and trends of total GPP losses. The presented error bars in (**a**–**d**) indicate one standard deviation between GPP datasets. The pink shading in (**e**, **f**) indicate the 95% confidence range for the fitted linear model. The results are based on GPP products and extreme indices with removed linear trend, 5-year moving windows as well as GLEAM soil moisture.

midlatitudes, while increasing losses related to drought-cold extremes are also detected in the early part of the growing season (Supplementary Fig. S16a). The drought-cold extremes impacts in spring can induce direct and lagged negative effects[39], and subsequent summers may suffer from persistent water deficit stress from drought and heat, consequently leading to increased losses in northern midlatitudes. In the pantropics, GPP losses associated with hydroclimatic extremes tend to decrease in most months without any clear seasonal patterns (Supplementary Fig. S16b).

Impacts on specific vegetation types and their changes. The vegetation type can modulate the influence of hydroclimatic extremes on GPP[16]. An analysis stratified by vegetation types reveals consistent large GPP losses associated with drought-heat, drought, drought-cold, and heat extremes in cropland, evergreen broadleaved forest, grassland, and shrubland (Fig. 4a, c and Supplementary Fig. S17a–g), suggesting a high vulnerability of these land cover types to these hydroclimatic extremes. In addition, drought-cold and cold extremes show strong impacts on evergreen needleleaf forests and mixed forests in high latitudes, where vegetation growth is highly controlled by temperature variations[40]. A certain amount of GPP losses is associated with extremely wet conditions across evergreen needleleaf forests and mixed forests, indicating the important role of wet extremes in affecting vegetation productivity in these two land cover types[41]. The trend analyses for specific vegetation types indicate the increase in GPP losses associated with drought-heat, drought-cold, drought, and heat extremes across croplands (Fig. 4b). In addition, the magnitudes of the increased trends are higher than those associated with decreased trends (Fig. 4b). These results imply an increasing stress of hydroclimatic extremes to cropland vegetation productivity. In contrast, GPP losses associated with hydroclimatic extremes show an overall decrease for evergreen broadleaf forests (Fig. 4d).

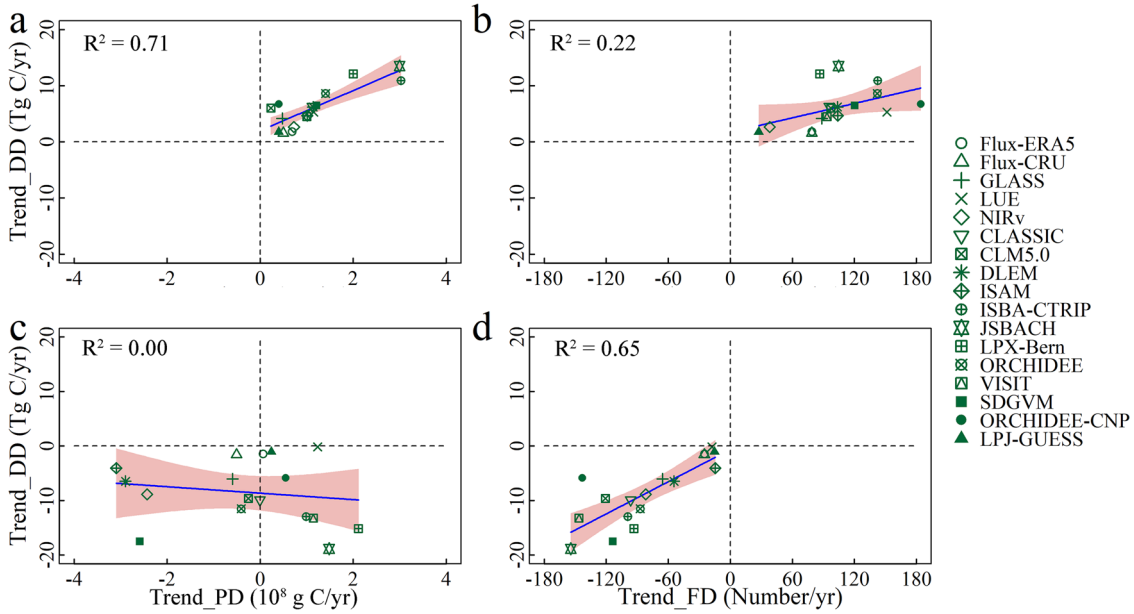

Fig. 3 Drivers of the trends in GPP losses associated with hydroclimatic extremes. a The changes in the magnitude of GPP loss per event associated with dominant drivers (*x*-axis) against GPP loss trends associated with dominant drivers (y-axis) in northern midlatitudes. **b** The changes in frequency of GPP loss related to dominant drivers (*x*-axis) against GPP loss trends associated with dominant drivers (*y*-axis) in northern midlatitudes. **c**, **d** The same as (**a**, **b**), but for pantropics. In (**a**) and (**c**), Trend_PD (x-axis label) refers to the change in the magnitude of GPP loss per event associated with dominant drivers. In (**b**) and (**d**), Trend_FD (*x*-axis label) refers to the change in frequency of GPP loss events related to dominant drivers. The pink shading indicates the 95% confidence range for the fitted linear model. The results are based on GPP products and extreme indices with removed linear trend, 5-year moving windows as well as GLEAM soil moisture.

The identified adverse impacts of hydroclimatic extremes on GPP across croplands could be potentially alleviated through management measures, such as irrigation and fertilization. To investigate this question, an additional set of model simulations without enabled land use management (TRENDY S2) was compared with the above-used model simulations, which include land use management (TRENDY S3) (Methods). Results indicate lower GPP losses in the simulations that additionally considered land use management in comparison to the models only driven by climate and CO_2 datasets (Fig. 4e). This result implies that land management options such as irrigation and fertilization could alleviate the adverse impact of hydroclimatic extremes on cropland GPP losses to some extent. However, the trends and magnitudes of changes in GPP losses with and without considering land use management show only a small difference ($P = 0.18$ for a two-sided t-test) and are strongly correlated across models ($r^2 = 0.78$, Fig. 4f). Moreover, for the simulations with enabled land management, the magnitude of increasing trends is on average 15.8% higher than that of decreasing trends in croplands. These results suggest that the present land management practices might be limited in their ability to reverse the increasingly adverse impacts of hydroclimatic extremes on GPP losses over croplands.

In summary, these results suggest a high vulnerability of cropland vegetation productivity to drought-heat, drought, drought-cold, and heat extremes, and that improving the ability to cope with impacts of hydroclimatic extremes through adequate management practices over croplands may be required.

Discussion

The effect of hydroclimatic impacts on GPP has been the topic of numerous studies worldwide during the past decades[17, 42, 43]. Many studies have analyzed the impact of droughts or heatwaves on regional or global GPP and mostly concluded that severe droughts or heatwaves cause significant GPP losses[44–46]. Notably drought-induced GPP losses have been detected in many regions such as North America[47, 48], Europe[49, 50], Inner Asia[51], and Australia[52]. However, whether terrestrial GPP losses associated with hydroclimatic extremes (droughts, extremely wetness, heatwaves and cold spells, as well as the corresponding compound extremes) during the past three and half decades are becoming more or less remains unclear. The conclusions on the GPP response to hydroclimatic extremes are subject to large uncertainties due to the varying sensitivities of different types of terrestrial ecosystems to hydroclimatic extremes[7, 53]. Moreover, which extreme events are significantly associated with GPP losses received limited attention, since most studies focus on individual droughts or heatwaves. Our analysis based on observationally-constrained and state-of-the-art modeled GPP datasets over multiple decades show a widespread strengthening and weakening of GPP losses associated with the identified significant hydroclimatic extreme drivers (i.e., drought-heat extremes, drought-cold extremes, drought, and heat extremes) across global terrestrial ecosystems. The strongest regional imprints are found in the northern midlatitudes (23.5-65°N) and pantropics (23.5°S-23.5°N).

Our result suggested that negative impacts associated with drought-heat extremes, drought, and heat extremes across the pantropics are decreasing, contributing to a weakening of GPP losses. This is consistent with previous studies that suggested that the future magnitude of extreme GPP losses could be projected to decrease due to elevated CO_2 concentration[4, 38, 54]. Our results suggest that the projected reduction in GPP losses associated with hydroclimatic extremes in the pantropics may already be underway. A higher partial pressure of CO_2 can stimulate photosynthesis and reduce stomatal conductance[55], leading to decreased water use and soil water savings[56, 57]. The elevated CO_2 thus can boost vegetation growth and enhance ecosystem productivity[58, 59]. In addition, the tendency towards positive or negative responses to hydroclimatic extremes could be modulated by vegetation types[16]. Extensive forests in the pantropics with deep and strong roots can obtain more groundwater from the

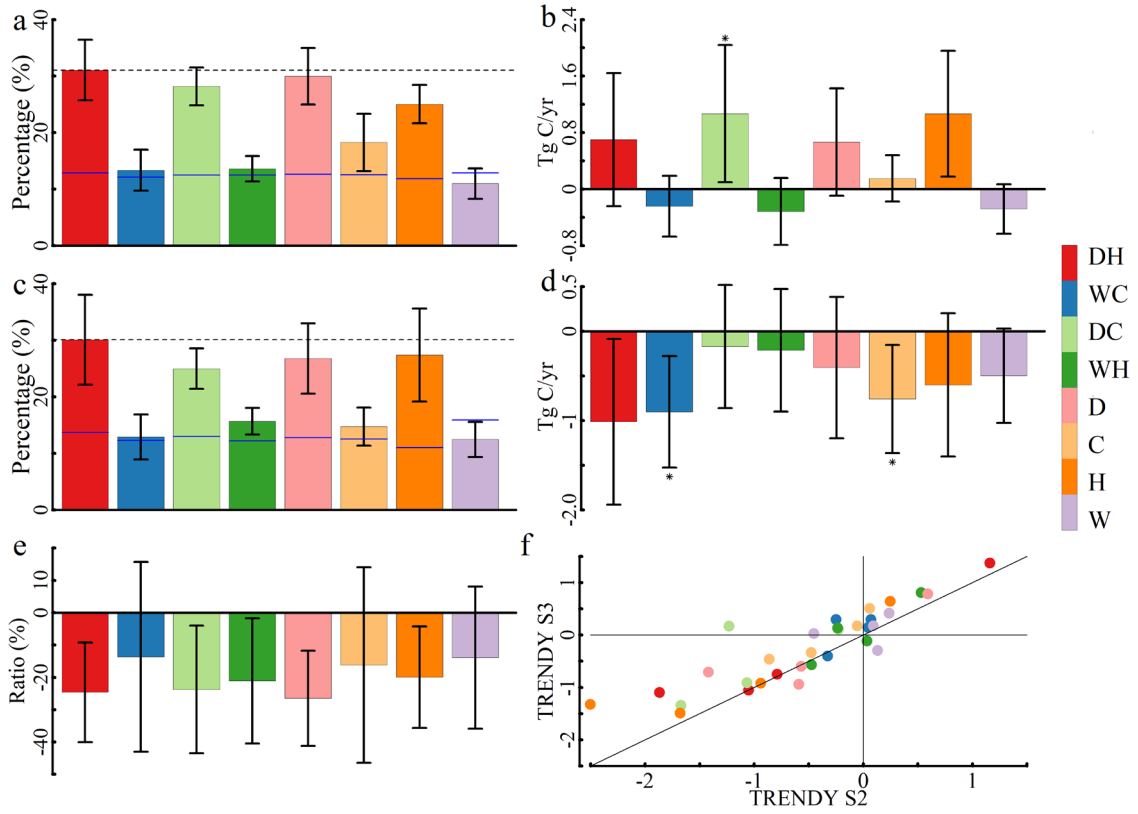

Fig. 4 Comparison and changes in GPP losses for specific land cover types from 1982-2016. a The GPP losses associated with hydroclimatic extremes in cropland. **b** The temporal trends of GPP losses in cropland associated with a certain hydroclimatic extreme. **c**, **d** The same as (**a**, **b**), but for evergreen broad-leaved forest. **e** The GPP losses difference between TRENDY S2 (no management) and S3 (with management) simulations. **f** Scatterplot for temporal trends (Tg C/yr) of cropland GPP losses associated with each hydroclimatic extreme between TRENDY S2 (no management) and S3 (with management) simulations. In (**e**) the ratio was computed as the difference between S3 and S2 simulation divided by the S3 simulation, and the presented error bars indicate one standard deviation between GPP products. In (**a**) and (**c**), blue lines within the bar indicate the 0.05 significant level. WC wet-cold extreme, WH wet-heat extreme, C cold extreme, W wet extreme. For details on the barplot see caption of Fig. 2.

deeper soil and are likely less affected by heatwaves and short-term drought stress[60, 61]. Forests thus seem to present higher resilience to drought and heat anomalies, which is reflected in a potential positive GPP anomalies during the events[62]. Moreover, GPP usually can recover to the normal state due to high resistance and resilience to extremes, suggesting that irreversible damage associated with extremes might not occur[17]. However, vegetation productivity could be impaired due to the future increase of temperatures above optimal temperature thresholds[63]. Ambient air is often warmer than the optimal temperature in the tropics. Consequently, future warming is not beneficial for plant productivity and carbon uptake[48]. Global warming is projected to decrease GPP[64], and the negative effects could outweigh CO_2 fertilization, especially for the Amazon region[65].

The situation is very different and much more worrisome in the northern midlatitudes, where GPP losses associated with drought-heat extremes, drought-cold extremes, drought, and heat extremes are already increasing. Widespread warmer temperatures may decrease soil water availability across most northern hemisphere[66], and sustained soil water deficit causes sensible heat increase, enhancing the heating of the near-surface air. The enhanced feedback between temperature and soil water further exacerbates the severity of compound drought-heat extremes in northern regions[67]. An increase in drought-heat severity can interfere with numerous biochemical and physiological processes of ecosystems, including photosynthesis, respiration, as well as nitrogen and protein metabolisms[68]. Enhanced drought-heat anomalies can also indirectly influence ecosystem productivity by increasing pest and disease infestations. Moreover, frequent droughts and heatwaves can increase vegetation damage and even result in mortality due to hydraulic failure or carbon starvation. When the increase in frequency and intensity of extremes outruns the vegetation's adaptive or acclimation capacities, additional reduction in productivity are likely to occur and even vegetation productivity experiences substantial changes in some cases[69]. In addition, rapid Arctic warming has resulted in the dramatic melting of Arctic Sea ice, potentially leading to more frequent and intense cold spells in early spring and autumn over most of the northern hemisphere[13, 25]. Drought-cold spring conditions can pose direct and lagged negative impacts on plant productivity by leaf frostbite, shortening growing season, and nutrient storage[70], and together with adverse synergistic effects and increasing subsequent summer drought-heat events[39], raising GPP losses in northern midlatitudes. The increasing impacts of the identified dominant extremes on GPP in the northern midlatitudes could threaten the stability and balance of global carbon gross update.

Our results further indicate the increasingly adverse impacts from the dominant extreme hydroclimatic drivers on crop productivity, and that such negative effects might not be tackled with current land management options. The hydroclimatic extremes usually result in large productivity reduction in croplands. This is due to the fact that crop systems are known to be very directly vulnerable to hydroclimatic extremes, which can lead to increased mortality and function collapse[71]. Therefore, our results suggest that investments in mitigation measures to improve the adaptive capacity and resilience of agricultural systems may be required. Overall, our study

demonstrates changing vulnerabilities of photosynthetic carbon uptake to different types of hydroclimatic extremes across regions.

Methods

GPP data. Five long-term monthly global GPP datasets from 1982 to 2016 were utilized in this study.

First, we used GPP (8 km spatial resolution) based on the satellite-driven light use efficiency approach (LUE) driven by time-varying satellite GIMMS FPAR3g and CRUNCEP v.8 meteorological forcing (here abbreviated as LUE GPP[33]). The GPP was improved with optimized spatially and temporally explicit LUE values derived from selected FLUXNET tower site data. Second, the FLUXCOM GPP (0.5° spatial resolution), which was produced by upscaling of local eddy covariance carbon flux tower measurements to global fields via machine learning methods. In this product, the interannual variability and trend patterns are derived from time-varying ERA5 or CRU meteorological input variables exclusively (here abbreviated as Flux-ERA5 and Flux-CRU GPP), while the seasonal cycle of plant growth is constrained by satellite vegetation data[35]. Third, we used GPP from satellite-based NIRv. NIRv, which is available at a 0.05° spatial resolution and monthly scale, is a newly developed satellite vegetation index that combines NDVI and near-infrared band reflectivity of vegetation and is a well-recognized proxy of GPP. This product was produced by upscaling the relationship between NIRv and observed GPP to the global scale and was judged to perform well in capturing the seasonal and inter-annual trends of GPP associated with climate variability and atmospheric CO_2 variation[34]. Fourth, we use the GLASS GPP (0.05° spatial resolution, 8-day temporal resolution), computed from the eddy covariance-LUE (EC-LUE) model driven by time-varying GLASS leaf area index. In the EC-LUE model, the regulations of several major environmental variables (i.e., atmospheric CO_2 concentration, radiation components, and atmospheric vapor pressure deficit) were integrated. The product reproduces well interannual variations and long-term trends of GPP[72]. Overall, the above introduced GPP dataset have all been validated with in-situ FLUXNET dataset and show good agreement with independent observations[33–35, 72].

Fifth, we employed GPP data from 12 process-based terrestrial biosphere models participating in the TRENDY v.9 multi-model intercomparison[36]. The GPP data in the TRENDY v.9 ensemble used in this study is based on simulations with CLASSIC, CLM5.0, DLEM, ISAM, ISBA-CTRIP, JSBACH, LPX-Bern, LPJ-GUESS, ORCHIDEE, ORCHIDEE-CNP, SDGVM, and VISIT. TRENDY simulation S3 that was forced by time-varying atmospheric CO_2, climate and land use was used in this study to analyze GPP losses associated with hydroclimatic extremes. The TRENDY GPP ensemble analyzed in this study consisted of 12 GPP members. In addition, to estimate the potential of land management activities to mitigate the impact of hydroclimatic extremes over croplands, such as irrigation and fertilization, we compared TRENDY simulation S3 with land use management and TRENDY simulation S2 only forced by climate and CO_2. The specific products include CLM 5.0, DLEM, ISAM, and LPJ-GUESS. Notably, irrigation in TRENDY is often implicit, by assuming no plant water stress/zero root zone water deficit, and this may be considered optimal irrigation management (that is, represent the maximum potential mitigation ability through elevating soil water deficit).

Hydroclimatic data. We used gridded monthly temperature and soil moisture to compute compound and individual hydroclimatic extreme indices. Temperature data (0.5° spatial resolution and monthly scale) were obtained from the Climatic Research Unit Time Series 4.05[73]. Root-zone soil moisture was obtained from the Global Land Evaporation Amsterdam Model (GLEAM)[74]. The GLEAM soil moisture has a 0.25° spatial resolution with monthly time step, and is strongly constrained by observations through assimilating multisource satellite-observed soil moisture, vegetation optical depth, and snow water equivalents from different satellite sensors[74]. We utilized the GLEAM soil moisture for the analyses shown in the main text. In addition, to test the impacts of different soil moisture products on our results, we also used the root-zone soil moisture from GLDAS catchment land surface model and ECMWF Reanalysis v5 (ERA5), which both have 0.25° resolution and monthly scale. GLDAS used data assimilation to incorporate satellite and observation in advanced land surface models to generate optimum land surface states and fluxes[75]. For ERA5, the third layer (28–100 cm) soil moisture was employed as this study focuses on extreme events that usually cause the reduction in soil moisture in deep layers. The two soil moisture products show well agreement with the independent observations[75, 76].

Land cover data. We used two types of land cover dataset, i.e., MODIS MCD12Q1 (500 meter spatial resolution) from 2001-2016 and the Climate Change Initiative product (300 meter spatial resolution) from 1992–2015[77], to mask the grids with extensive land cover change. The definition of extensive land cover change area is that the maximum changed land cover area between two consecutive years was larger than 20% of the total area in a 0.5° pixel[65]. Only a few grid cells (<1%) were detected at the coarse target resolution (0.5°) and were consequently masked in the final land-cover map applied in this study (Supplementary Fig. S18). These masked areas have been excluded from the land-cover analyses and all presented results in the manuscript. In addition, land cover data in 2016 from MCD12Q1 product was employed to analyze the impacts of hydroclimatic extremes on GPP losses over different vegetation types. In line with the International Geosphere-Biosphere Programme classification, the original land cover classes were aggregated into evergreen needleleaf forests, evergreen broadleaf forests, deciduous needleleaf forests, deciduous broadleaf forests, mixed forests, shrublands, savannas, grassland, and cropland, with 0.5° spatial resolution. The spatial pattern of land use cover used in this study is shown in Supplementary Fig. S18.

The fine-scale and/or coarse-scale spatial dataset used in this study were all resampled to 0.5° spatial resolution using bilinear interpolation.

Detection of GPP losses and attribution of hydroclimatic extremes

Detection of GPP losses. As the focus was to investigate GPP losses, the linear (or non-linear) trend was first removed from all GPP datasets individually to avoid misleading results due to a regional positive (or negative) trend induced by CO_2 concentration and climate change that shifts the overall mean. Non-linear trends were obtained via smoothing splines, which was implemented by using losses function in the R language. Additionally, as GPP shows distinguishable seasonality, the seasonal cycle at annual scale was subtracted from all datasets for each grid cell individually by using the seasonal-trend decomposition procedure based on loess. In general, local negative GPP extremes (hereafter termed GPP losses throughout the manuscript) were detected using the tenth percentile threshold of the local de-trended and de-seasonalized GPP time series at grid cell level (a common and standard for detecting GPP loss[18]), and further classified according to the occurrence of anomalies below the threshold.

Attribution of hydroclimatic extreme drivers. Since droughts, extremely wet conditions, heats and cold spells, as well as the corresponding compound events (drought-heat, drought-cold, wet-cold extremes, and wet-heat extremes) are frequently recurring hydroclimatic extremes, the identified GPP loss events were then attributed to these potential hydroclimatic extreme drivers.

To capture individual hydroclimatic extremes (i.e., droughts, wet extremes, heat extremes, and cold extremes), standardized temperature index (STI) and standardized soil moisture index (SSMI) were utilized in this study, so that allowing for a comparison of hydroclimatic anomalies across different climatic regions and seasons. The STI was applied to identify cold and heat extremes, while the SSMI was employed to characterize drought and wet extremes.

Building on earlier studies[39, 78, 79], the two univariate indices incorporating both soil moisture and temperature were used to identify compound events via a compound drought-heat index (CDHI) and a compound drought-cold index (CDCDI). CDHI generally describes variations from compound drought-heat conditions to compound extreme wet-cold conditions, while CDCI from compound drought-cold conditions to compound extreme wet-heat conditions. By considering compound conditions, the two indices can better explain vegetation productivity dynamic associated with hydroclimatic anomalies than typical univariate indices (e.g., STI or SSMI individually)[39]. Estimating the probability distribution is required to compute the indices. Here, to avoid making assumption on the most suitable theoretical distribution, we computed the indices based on an empirical cumulative distribution function. A detailed description of the two compound event indices can be found in the study of Li et al. [39]. The pronounced trend of hydroclimatic variables can induce confounding positive (or negative) impacts on GPP[80]. Following previous studies[18, 80], the linear (or non-linear) trend of the compound and univariate indices used in this study were thus removed at each grid cell. We used 3-month compound and individual indices so that they can capture the short-term water deficit[81]. In addition, we note that the compound and univariate indices follow the normal distribution, and thus the frequency of extremes identified by compound and univariate indices are identical.

The GPP loss events were attributed to hydroclimatic extremes on the basis of coinciding significant climate anomalies[18]. A GPP loss event was attributed to a potential driver if two criteria are met, i.e., at least one coinciding significant (i) extreme anomaly ($P \le 0.1$, or $P \ge 0.9$) and (ii) a mean anomaly ($P \le 0.3$, or $P \ge 0.7$) were detected within the three months preceding the GPP event. The first criterion is to ensure that there is at least one significant extreme anomaly that induced a GPP loss. However, hydroclimatic anomaly conditions during some months might be substantial while those during other months can decay due to temporary recovery of hydroclimatic conditions[82]. Therefore, abnormal mean hydroclimatic conditions ($P \le 0.3$, or $P \ge 0.7$) indicate lingering impacts after significant hydroclimatic extremes[83] or precondition anomalies preceding significant hydroclimatic extremes[84], ensuring an overall hydroclimatic anomaly. Given the possible lagged responses of vegetation ecosystems to hydroclimatic extremes[70, 85], we consider a maximum of three months prior to the GPP event to detect hydroclimatic anomalies. For example, a GPP loss was attributed to heat extreme if at least one significant ($P \ge 0.9$) anomalous STI value and mean ($P \ge 0.7$) anomalous STI value within three months preceded this GPP loss.

Notably, multiple hydroclimatic extreme drivers can be anomalous during a GPP loss event and thus can be counted toward the attribution of that event. For example, if coinciding anomalies in drought and heat were detected, the corresponding GPP event was assigned to both. The attribution analyses were conducted for each GPP dataset. The presented results throughout the manuscript were derived as the mean of the results of all GPP dataset, and the error bars indicated by one standard deviation show uncertainty between GPP dataset. In addition, we used percentiles to represent the magnitude of GPP losses associated

with hydroclimatic extremes, which can provide a more intuitive understanding of the impact of hydroclimatic extremes on GPP. For trend analysis, we present the actual change in GPP loss values.

Statistical analysis. Bootstrapping-based significance test[86] is applied for each hydroclimatic extreme driver to asses whether the association between the driver and the GPP loss is significant. We test the null hypothesis that a hydroclimatic extreme caused GPP loss in each grid cell can be reproduced by chance. Thereby, we used the bootstrapping method to generate 1000 alternative time series of an extreme index in each grid cell, and then attributed the GPP losses to the hydroclimatic extreme based on the resampled timeseries and above attribution method. If observed GPP losses are higher than 95% of the 1000 resampled datasets (this corresponds to a p value of 0.05 or below) at a specific grid cell or a specific region, the result is considered statistically significant.

To investigate the changes in hydroclimatic extreme impacts, the trend and statistical significance of GPP losses associated with hydroclimatic extremes were analyzed for each GPP dataset and each vegetation type using the Mann-Kendall trend test. We used a 5-year moving window in our trends analysis to smooth out time series fluctuations and highlight trends. 10-year and 15-year moving windows were also applied in this study to evaluate the robustness of the trend analyses. Moreover, to estimate the potential of land management activities to mitigate the impact of hydroclimatic extremes over croplands, the impact difference associated with hydroclimatic extremes between TRENDY S2 and S3 simulations in cropland was computed for specific products (i.e., CLM 5.0, DLEM, ISAM, and LPJ-GUESS).

In addition, we explored the mechanism responsible for the asymmetrical changes in GPP losses attributed to hydroclimatic extremes between northern midlatitudes (23.5-65°N) and pantropics (23.5°S-23.5°N). To this end, we first counted the frequency of GPP losses associated with the dominant hydroclimatic extreme drivers (drought-heat, drought-cold, drought, and heat) over 5-years moving windows, and then computed the trends in these counts via the Mann-Kendall trend test (Fig. 3). Similarly, we computed the average magnitude of the GPP losses associated with the dominant hydroclimatic extreme drivers over individual 5-years moving windows, and then computed associated trends.

The flow diagram for analyzing GPP losses associated with hydroclimatic extremes is shown in Supplementary Fig. S19.

Data availability

Model outputs generated by TRENDY v9 ecosystem models are available from Stephen Stich (s.a.sitch@exeter.ac.uk) or Pierre Friedlingstein (p. friedlingstein@exeter.ac.uk) upon request. The MODIS land-cover maps are available at https://lpdaac.usgs.gov/products/mcd12q1v006/; The climatic variables from the CRU TS4.03 data are available at https://crudata.uea.ac.uk/cru/data/hrg/; The soil moisture from the GLEAM v3.2a data is available at https://www.gleam.eu/; The soil moisture from the GLDAS is available at https://disc.gsfc.nasa.gov/datasets?page=1; The ERA5 soil moisture is available at https://cds.climate.copernicus.eu/cdsapp#!/search?type=dataset. The data to reproduce the main results presented can be accessed from https://doi.org/10.6084/m9.figshare.22817252.

Received: 25 November 2022; Accepted: 26 May 2023;
Published online: 02 June 2023

References

1. Brienen, R. J. W. et al. Long-term decline of the Amazon carbon sink. *Nature* **519**, 344–348 (2015).
2. Le Quéré, C. et al. Trends in the sources and sinks of carbon dioxide. *Nat. Geosci.* **2**, 831–836 (2009).
3. Xu, C. et al. Increasing impacts of extreme droughts on vegetation productivity under climate change. *Nat. Clim. Chang.* **9**, 948–953 (2019).
4. Gampe, D. et al. Increasing impact of warm droughts on northern ecosystem productivity over recent decades. *Nat. Clim. Change* 1–8 https://doi.org/10.1038/s41558-021-01112-8 (2021).
5. Zhao, M. & Running, S. W. Drought-induced reduction in global terrestrial net primary production from 2000 through 2009. *Science* **329**, 940–943 (2010).
6. Zeng, N., Qian, H., Roedenbeck, C. & Heimann, M. Impact of 1998–2002 midlatitude drought and warming on terrestrial ecosystem and the global carbon cycle. *Geophys. Res. Lett.* **32**, L22709 (2005).
7. Piao, S. et al. The impacts of climate extremes on the terrestrial carbon cycle: a review. *Sci. China Earth Sci.* **62**, 1551–1563 (2019).
8. Reichstein, M. et al. Climate extremes and the carbon cycle. *Nature* **500**, 287–295 (2013).
9. Touma, D. et al. Climate change increases risk of extreme rainfall following wildfire in the western United States. *Sci. Adv.* **8**, eabm0320 (2022).
10. Gudmundsson, L. et al. Globally observed trends in mean and extreme river flow attributed to climate change. *Science* **371**, 1159–1162 (2021).
11. Seneviratne, S. I. et al. Weather and climate extreme events in a changing climate. In *Climate Change 2021: The Physical Science Basis. Contribution of Working Group I to the Sixth Assessment Report of the Intergovernmental Panel on Climate Change*, pp. 1513–1766 (2021).
12. Wentz, F. J., Ricciardulli, L., Hilburn, K. & Mears, C. How much more rain will global warming bring? *Science* **317**, 233–235 (2007).
13. Tang, R. et al. Increasing terrestrial ecosystem carbon release in response to autumn cooling and warming. *Nat. Clim. Chang.* **12**, 380–385 (2022).
14. Pan, S. et al. Climate extreme versus carbon extreme: responses of terrestrial carbon fluxes to temperature and precipitation. *J. Geophys. Res. Biogeosci.* **125**, e2019JG005252 (2020).
15. Chen, T. et al. A global analysis of the impact of drought on net primary productivity. *Hydrol. Earth Syst. Sc.* **17**, 3885–3894 (2013).
16. Flach, M. et al. Vegetation modulates the impact of climate extremes on gross primary production. *Biogeosciences* **18**, 39–53 (2021).
17. Xu, H., Xiao, J. & Zhang, Z. Heatwave effects on gross primary production of northern mid-latitude ecosystems. *Environ. Res. Lett.* **15**, 074027 (2020).
18. Zscheischler, J., Mahecha, M. D., Harmeling, S. & Reichstein, M. Detection and attribution of large spatiotemporal extreme events in Earth observation data. *Ecol. Inform.* **15**, 66–73 (2013).
19. Sippel, S. et al. Drought, heat, and the carbon cycle: a review. *Curr. Clim. Change Rep.* **4**, 266–286 (2018).
20. Zscheischler, J. et al. Impact of large-scale climate extremes on biospheric carbon fluxes: An intercomparison based on MsTMIP data. *Glob. Biogeochem. Cycles* **28**, 585–600 (2014).
21. Bastos, A. et al. Direct and seasonal legacy effects of the 2018 heat wave and drought on European ecosystem productivity. *Sci. Adv.* **6**, eaba2724 (2020).
22. Wei, X. et al. Global assessment of lagged and cumulative effects of drought on grassland gross primary production. *Ecolo. Indic.* **136**, 108646 (2022).
23. He, Q. et al. Drought risk of global terrestrial gross primary productivity over the last 40 years detected by a remote sensing-driven process model. *J. Geophys. Res. Biogeosci.* **126**, e2020JG005944 (2021).
24. Johnson, N. C., Xie, S.-P., Kosaka, Y. & Li, X. Increasing occurrence of cold and warm extremes during the recent global warming slowdown. *Nat. Commun.* **9**, 1724 (2018).
25. Cohen, J. et al. Recent Arctic amplification and extreme mid-latitude weather. *Nat. Geosci.* **7**, 627–637 (2014).
26. Qun, G. et al. Contrasting responses of gross primary productivity to precipitation events in a water-limited and a temperature-limited grassland ecosystem. *Agric. For. Meteorol.* **214–215**, 169–177 (2015).
27. Wu, X. et al. Differentiating drought legacy effects on vegetation growth over the temperate Northern Hemisphere. *Glob. Change Biol.* **24**, 504–516 (2018).
28. Phillips, O. L. et al. Drought sensitivity of the Amazon Rainforest. *Science* **323**, 1344–1347 (2009).
29. Wang, Y., Fu, Z., Hu, Z. & Niu, S. Tracking global patterns of drought-induced productivity loss along severity gradient. *J. Geophys. Res. Biogeosci.* **127**, e2021JG006753 (2022).
30. Jiao, W. et al. Observed increasing water constraint on vegetation growth over the last three decades. *Nat. Commun.* **12**, 3777 (2021).
31. Anderegg, W. R. L., Trugman, A. T., Badgley, G., Konings, A. G. & Shaw, J. Divergent forest sensitivity to repeated extreme droughts. *Nat. Clim. Chang.* **10**, 1091–1095 (2020).
32. Yu, Z. et al. Global gross primary productivity and water use efficiency changes under drought stress. *Environ. Res. Lett.* **12**, 014016 (2017).
33. O'Sullivan, M. et al. Climate-driven variability and trends in plant productivity over recent decades based on three global products. *Glob. Biogeochem. Cycles* **34**, e2020GB006613 (2020).
34. Wang, S., Zhang, Y., Ju, W., Qiu, B. & Zhang, Z. Tracking the seasonal and inter-annual variations of global gross primary production during last four decades using satellite near-infrared reflectance data. *Sci. Total Environ.* **755**, 142569 (2021).
35. Jung, M. et al. Scaling carbon fluxes from eddy covariance sites to globe: synthesis and evaluation of the FLUXCOM approach. *Biogeosciences* **17**, 1343–1365 (2020).
36. Friedlingstein, P. et al. Global carbon budget 2020. *Earth Syst. Sci. Data* **12**, 3269–3340 (2020).
37. Luo, X. & Keenan, T. F. Tropical extreme droughts drive long-term increase in atmospheric CO2 growth rate variability. *Nat. Commun.* **13**, 1193 (2022).
38. Zscheischler, J. et al. Carbon cycle extremes during the 21st century in CMIP5 models: Future evolution and attribution to climatic drivers. *Geophys. Res. Lett.* **41**, 8853–8861 (2014).
39. Li, J. et al. Regional asymmetry in the response of global vegetation growth to springtime compound climate events. *Commun. Earth Environ.* **3**, 1–9 (2022).
40. Observed increasing water constraint on vegetation growth over the last three decades. *Nat. Comm.* **12**, 3777 (2021)
41. Famiglietti, C. A., Michalak, A. M. & Konings, A. G. Extreme wet events as important as extreme dry events in controlling spatial patterns of vegetation greenness anomalies. *Environ. Res. Lett.* **16**, 074014 (2021).

42. Cao, D. et al. Projected increases in global terrestrial net primary productivity loss caused by drought under climate change. *Earth's Future*, **10**, e2022EF002681 (2022).
43. Zhang, Z., Ju, W., Zhou, Y. & Li, X. Revisiting the cumulative effects of drought on global gross primary productivity based on new long-term series data (1982–2018). *Glob. Change Biol.* **28**, 3620–3635 (2022).
44. Zhang, Y. et al. Canopy and physiological controls of GPP during drought and heat wave. *Geophys. Res, Lett,* **43**, 3325–3333 (2016).
45. Yang, H. et al. The detection and attribution of extreme reductions in vegetation growth across the global land surface. *Glob. Change Biol.* **29**, 2351–2362 (2023).
46. Hwang, T. et al. Evaluating drought effect on MODIS Gross Primary Production (GPP) with an eco-hydrological model in the mountainous forest, East Asia. *Glob. Change Biol.* **14**, 1037–1056 (2008).
47. He, W. et al. Large-scale droughts responsible for dramatic reductions of terrestrial net carbon uptake over North America in 2011 and 2012. *J. Geophys. Res. Biogeosci.* **123**, 2053–2071 (2018).
48. Wang, T. et al. Emerging negative impact of warming on summer carbon uptake in northern ecosystems. *Nat. Commun.* **9**, 5391 (2018).
49. Ciais, P. et al. Europe-wide reduction in primary productivity caused by the heat and drought in 2003. *Nature* **437**, 529–533 (2005).
50. Fu, Z. et al. Sensitivity of gross primary productivity to climatic drivers during the summer drought of 2018 in Europe. *Philos. Trans. R. Soc. B: Biol. Sci.* **375**, 20190747 (2020).
51. Poulter, B. et al. Recent trends in Inner Asian forest dynamics to temperature and precipitation indicate high sensitivity to climate change. *Agric. For. Meteorol.* **178–179**, 31–45 (2013).
52. Gobron, N., Belward, A., Pinty, B. & Knorr, W. Monitoring biosphere vegetation 1998–2009. *Geophys. Res. Lett.* **37**,L15402 (2010).
53. Xinyao, X. et al. Uncertainty analysis of multiple global GPP datasets in characterizing the lagged effect of drought on photosynthesis. *Ecol. Indic.* **113**, 106224 (2020).
54. Tian, C. et al. Projections of changes in ecosystem productivity under 1.5 °C and 2 °C global warming. *Glob. Planet. Change* **205**, 103588 (2021).
55. Leakey, A. D. B. et al. Elevated CO2 effects on plant carbon, nitrogen, and water relations: six important lessons from FACE. *J. Exp. Bot.* **60**, 2859–2876 (2009).
56. Fatichi, S. et al. Partitioning direct and indirect effects reveals the response of water-limited ecosystems to elevated CO2. *Proc. Natl Acad. Sci.* **113**, 12757–12762 (2016).
57. Swann, A. L. S., Hoffman, F. M., Koven, C. D. & Randerson, J. T. Plant responses to increasing CO2 reduce estimates of climate impacts on drought severity. *Proc. Natl Acad. Sci.* **113**, 10019–10024 (2016).
58. Zhu, Z. et al. Greening of the Earth and its drivers. *Nat. Clim. Change* **6**, 791–795 (2016).
59. Cernusak, L. A. et al. Robust response of terrestrial plants to rising CO_2. *Trends Plant Sci.* **24**, 578–586 (2019).
60. Yi, K., Dragoni, D., Phillips, R. P., Roman, D. T. & Novick, K. A. Dynamics of stem water uptake among isohydric and anisohydric species experiencing a severe drought. *Tree Physiol.* **37**, 1379–1392 (2017).
61. Ruehr, N. K., Gast, A., Weber, C., Daub, B. & Arneth, A. Water availability as dominant control of heat stress responses in two contrasting tree species. *Tree Physiol.* **36**, 164–178 (2016).
62. Li, J., Wang, Z. & Lai, C. Severe drought events inducing large decrease of net primary productivity in mainland China during 1982–2015. *Sci. Total Environ.* **703**, 135541 (2020).
63. Zhang, Y. et al. Future reversal of warming-enhanced vegetation productivity in the Northern Hemisphere. *Nat. Clim. Chang.* **12**, 581–586 (2022).
64. Song, C. et al. Continental-scale decrease in net primary productivity in streams due to climate warming. *Nat. Geosci.* **11**, 415–420 (2018).
65. Sang, Y. et al. Recent global decline of CO_2 fertilization effects on vegetation photosynthesis. *Science* **373**, 1295–1300 (2021).
66. Zscheischler, J. & Seneviratne, S. I. Dependence of drivers affects risks associated with compound events. *Sci. Adv.* **3**, 1–11 (2017).
67. Benson, D. O. & Dirmeyer, P. A. Characterizing the relationship between temperature and soil moisture extremes and their role in the exacerbation of heat waves over the contiguous United States. *J. Clim.* **34**, 2175–2187 (2021).
68. Anderegg, W. R. L., Kane, J. M. & Anderegg, L. D. L. Consequences of widespread tree mortality triggered by drought and temperature stress. *Nat. Clim. Change* **3**, 30–36 (2013).
69. Hammond, W. M. et al. Global field observations of tree die-off reveal hotter-drought fingerprint for Earth's forests. *Nat. Commun.* **13**, 1761 (2022).
70. Buermann, W. et al. Widespread seasonal compensation effects of spring warming on northern plant productivity. *Nature* **562**, 110–114 (2018).
71. Yang, Y. et al. Contrasting responses of water use efficiency to drought across global terrestrial ecosystems. *Sci. Rep.* **6**, 23284 (2016).
72. Zheng, Y. et al. Improved estimate of global gross primary production for reproducing its long-term variation, 1982–2017. *Earth Syst. Sci. Data* **12**, 2725–2746 (2020).
73. Harris, I., Jones, P. D., Osborn, T. J. & Lister, D. H. Updated high-resolution grids of monthly climatic observations—the CRU TS3.10 Dataset. *Int. J. Climatol.* **34**, 623–642 (2014).
74. Martens, B. et al. GLEAM v3: satellite-based land evaporation and root-zone soil moisture. *Geosci. Model Dev.* **10**, 1903–1925 (2017).
75. Rodell, M. et al. The global land data assimilation system. *Bull. Am. Meteorol.Soc.* https://doi.org/10.1175/BAMS-85-3-381 (2004).
76. Li, W. et al. Revisiting global vegetation controls using multi-layer soil moisture. *Geophys. Res. Lett.* **48**, e2021GL092856 (2021).
77. Bontemps, S. et al. Consistent global land cover maps for climate modelling communities: current achievements of the ESA's land cover CCI. *Proc. ESA living planet symposium, Edimburgh* **13**, 9–13 (2013).
78. Hao, Z., Hao, F., Singh, V. P. & Zhang, X. Statistical prediction of the severity of compound dry-hot events based on El Niño-Southern Oscillation. *J. Hydrol.* **572**, 243–250 (2019).
79. Li, J. et al. A standardized index for assessing sub-monthly compound dry and hot conditions with application in China. *Hydrol. Earth Syst. Sci.* **25**, 1587–1601 (2021).
80. Chen, W. et al. Negative extreme events in gross primary productivity and their drivers in China during the past three decades. *Agric. For. Meteorol.* **275**, 47–58 (2019).
81. Zhang, Y., Keenan, T. F. & Zhou, S. Exacerbated drought impacts on global ecosystems due to structural overshoot. *Nat. Ecol. Evol.* **5**, 1490–1498 (2021).
82. Li, J. et al. A new framework for tracking flash drought events in space and time. *CATENA* **194**, 104763 (2020).
83. Svoboda, M. et al. The drought monitor. *Bull. Am. Meteorol. Soc.* **83**, 1181–1190 (2002).
84. Zscheischler, J. et al. A typology of compound weather and climate events. *Nat. Rev. Earth Environ.* **1**, 333–347 (2020).
85. Lian, X. et al. Seasonal biological carryover dominates northern vegetation growth. *Nat. Commun.* **12**, 983 (2021).
86. Ridder, N. N. et al. Global hotspots for the occurrence of compound events. *Nat. Commun.* **11**, 5956 (2020).

Acknowledgements

J.L. would also like to thank Yao Zhang for fruitful conversations on the topic. The authors acknowledge the European COST Action DAMOCLES (CA17109). This project has received funding from the European Union's Horizon 2020 research and innovation program under grant agreement No 101003469. J.Z. acknowledges the Helmholtz Initiative and Networking Fund (Young Investigator Group COMPOUNDX, Grant Agreement VH-NG-1537). Z.W. acknowledges the National Natural Science Foundation of China (51879107,51709117), the Water Resource Science and Technology Innovation Program of Guangdong Province (2020-29), and the Guangdong Basic and Applied Basic Research Foundation (2019A1515111144). D.G. benefited from the ANR program CLAND (ANR-16-CONV-0003).

Author contributions

J.L., E.B., and J.Z. designed the research; J.L. performed analysis and drafted the paper; Z.W., S.S., V.A., A.A., A.J., D.G., and H.T. contributed to data analysis and interpretation. All authors edited the manuscript.

Funding

Open Access funding enabled and organized by Projekt DEAL.

Competing interests

The authors declare no competing interests.

Additional information

Supplementary information The online version contains supplementary material available at https://doi.org/10.1038/s43247-023-00869-4.

Correspondence and requests for materials should be addressed to Jakob Zscheischler.

Peer review information *Communications Earth & Environment* thanks the other, anonymous, reviewer(s) for their contribution to the peer review of this work. Primary Handling Editor: Aliénor Lavergne.